Structure of the lethal phage pinhole

Ting Pang[a], Christos G. Savva[b,c], Karen G. Fleming[d], Douglas K. Struck[a], and Ry Young[a,1]

[a]Department of Biochemistry and Biophysics, Texas A&M University, 2128 TAMU, College Station, TX 77843; [b]Microscopy and Imaging Center, Texas A&M University, 2257 TAMU, College Station, TX 77843; [c]Department of Biology, Texas A&M University, 3528 TAMU, College Station, TX 77843; and [d]Thomas C. Jenkins Department of Biophysics, Johns Hopkins University, 3400 North Charles Street, Baltimore, MA 21218

Edited by Thomas J. Silhavy, Princeton University, Princeton, NJ, and approved September 29, 2009 (received for review July 16, 2009)

Perhaps the simplest of biological timing systems, bacteriophage holins accumulate during the phage morphogenesis period and then trigger to permeabilize the cytoplasmic membrane with lethal holes; thus, terminating the infection cycle. Canonical holins form very large holes that allow nonspecific release of fully-folded proteins, but a recently discovered class of holins, the pinholins, make much smaller holes, or pinholes, that serve only to depolarize the membrane. Here, we interrogate the structure of the prototype pinholin by negative-stain transmission electron-microscopy, cysteine-accessibility, and chemical cross-linking, as well as by computational approaches. Together, the results suggest that the pinholin forms symmetric heptameric structures with the hydrophilic surface of one transmembrane domain lining the surface of a central channel ≈15 Å in diameter. The structural model also suggests a rationale for the prehole state of the pinholin, the persistence of which defines the duration of the viral latent period, and for the sensitivity of the holin timing system to the energized state of the membrane.

glycine zipper | holin | lysis | SAR domain | thiol modification

The most frequent cytocidal event in the biosphere is the holin-mediated permeabilization of the bacterial membrane that terminates the bacteriophage infection cycle (1). At an allele-specific time, the holin triggers to disrupt the cytoplasmic membrane by the formation of nonspecific holes, the first step in a three-step lytic process involving three other phage proteins, the endolysin and Rz-Rz1, the components of the spanin complex (1, 2). Besides deenergizing the membrane and bringing macromolecular synthesis to a halt, hole-formation allows the destruction of the murein layer by the endolysin, which in turn allows the disruption of the outer membrane by the spanin complex. The entire process is finished within seconds of triggering (3). The canonical holins, such as that of phage λ, form very large holes that allow fully-folded endolysins to pass through the membrane to attack the murein. These holes are nonspecific, allowing passage of unrelated endolysins (4), and large enough for 500-kDa proteins (5).

Recently, an alternative and remarkably different class of holin-endolysin systems has emerged (6–8). This class, represented by the lambdoid bacteriophage 21, utilizes endolysins having novel N-terminal secretory signals called signal-anchor release (SAR) domains. SAR sequences initially act as signal-anchor domains and promote the integration of proteins into the cytoplasmic membrane with type II, N-in, C-out topology (6, 9). Importantly, despite the fact that the muralytic domain of the SAR endolysins is secreted to the periplasm, these enzymes are catalytically inactive in their membrane-tethered state, which prevents premature lysis that would curtail the cytoplasmic assembly of progeny virions. Maintenance of the tethered, inactive state of the endolysin depends on the energized state of the bilayer, and release into the periplasm is quantitative when the holin triggers to disrupt the membrane. Thus, for SAR endolysins, the holin protein need only produce lesions large enough to allow the passage of ions through and depolarization of the cytoplasmic membrane. Indeed, unlike lesions formed by the λ holin, lesions formed by the phage 21 holin did not allow the passage of either λ endolysin or a periplasmic marker-tagged GFP protein (8). The term "pinholin" has been proposed to differentiate the small-hole (pinhole) forming character of the phage 21 holin from the canonical holins that form large, nonspecific holes. A focus on the molecular basis of pinholin function seems warranted, not only because of the intriguing functional differences with the canonical holins, but also because a homolog of the S^{21} pinholin has been shown to be involved in the programmed release of the Shiga-like toxin by enterohemorrhagic *Escherichia coli* O157:H7 (10, 11).

Like the λ holin gene *S*, the phage 21 holin gene, S^{21} encodes two proteins, $S^{21}71$ and $S^{21}68$, by virtue of alternate translational starts (Fig. 1*A*); the longer gene product, like that of lambda, has inhibitory character, and thus, is an antiholin (12). Analysis of $S^{21}68$, an allele that produces only the holin, has shown that despite its small size of 68 residues, the product has two functional domains corresponding to the two predicted transmembrane domains (TMDs) (Fig. 1*A*). TMD1 is not only dispensable for hole-formation and lysis, but in fact, is itself a SAR domain that must exit the bilayer in order for TMD2 to be competent for hole-formation (Fig. 1*B*) (7). This property is most dramatically illustrated by the modified allele $irsS^{21}68$, which encodes the $S^{21}68$ with the *irs* epitope, containing two positively-charged residues, added to the N terminus. Because the extra charges prevent TMD1 from exiting the membrane, the $irsS^{21}68$ protein has an absolute lysis-defective phenotype (7). In this article, we present biochemical, ultrastructural, and computational studies of the elements of $S^{21}68$ that are involved in the membrane lesion. The results are discussed in terms of a model for the structure of the pinhole and the implications for its temporally-scheduled formation.

Results

Detergent-Solubilized $S^{21}68$ Forms Channel-Like Structures. After purification in n-dodecyl-β-D-Maltopyranoside (DDM), $S^{21}68$ was found to form oligomers with an apparent size of 104 kDa in size-exclusion chromatography (Fig. 2*A*; Fig. S1). This size corresponds to complexes with 4–7 $S^{21}68$ molecules, based on a range of ≈100–140 for the aggregation number of DDM (13–16). Electron microscopy of negatively-stained $S^{21}68$ purified in DDM revealed small doughnut-shaped particles that were reasonably monodisperse (Fig. 2*B*). Reference-free classification of the $S^{21}68$ oligomers resulted in roughly spherical class averages that measured between 75 and 80 Å in diameter, with a central stain-filled cavity of ≈15 Å (see top row in Fig. 2*B Inset*). Some of these classes displayed a roughly hexagonal shape, although no symmetry had been imposed. Examination of structures formed by $S^{21}68_{\Delta TMD1}$ and by lysis-defective $irsS^{21}68$ resulted in particles with similar class averages. This result was not surprising for

Author contributions: T.P., C.G.S., D.K.S., and R.F.Y. designed research; T.P., C.G.S., and K.G.F. performed research; K.G.F. and R.Y. contributed new reagents/analytic tools; T.P., C.G.S., K.G.F., D.K.S., and R.Y. analyzed data; and T.P., C.G.S., and R.Y. wrote the paper.

The authors declare no conflict of interest.

This article is a PNAS Direct Submission.

[1]To whom correspondence should be addressed. E-mail: ryland@tamu.edu.

This article contains supporting information online at www.pnas.org/cgi/content/full/0907941106/DCSupplemental.

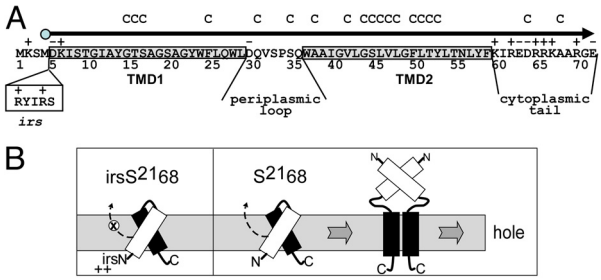

Fig. 1. Features of S^{21}68. (*A*) Sequence of the S^{21} reading frame. The 71 residues encoded by the *S^{21}* gene are shown, with the S^{21}68 reading frame, which begins with Met4, depicted by the arrowhead line. TMD1 and TMD2 are indicated by shaded boxes, and the regions corresponding to the periplasmic loop and cytoplasmic tail are so labeled. Residues altered to Cys for this study are indicated by C above the sequence. The *irs* epitope inserted after Met-4 in the irsS^{21}68 variant is shown in the clear box. (*B*) Model for pinhole formation by S^{21}68. TMD1 (white) is initially in the membrane, bound to TMD2 (black). When TMD1 exits the membrane, TMD2 is able to dimerize and then oligomerize, in the pathway to pinhole formation. TMD1 undergoes homotypic interactions in the periplasm that facilitate, but are not necessary, for pinhole formation. To the left, the inhibitory effect of the *irs* epitope, with its two positive charges, on the release of TMD1 from the membrane is depicted. Modified from Park et al. (7) with permission.

irsS^{21}68, because the membrane barrier that restrains the tagged TMD1 is removed by detergent. We suggest that the similarity in the negative-stain images between the oligomer of the full-length holin and that of S^{21}68$_{\Delta TMD1}$ reflects positioning of TMD1 in oligomeric bundles stacked over the pinhole (Fig. 1*B*).

Hole-Forming Ability of *S^{21}68* Alleles. The negative stain images of the purified pinholin suggest an oligomeric structure with a small channel, consistent with its biological function. To probe the structure of the pinholin in the membrane, we used a variation of cysteine-scanning-accessibility. This approach involves treating whole cells expressing the desired *S^{21}68* single-cysteine

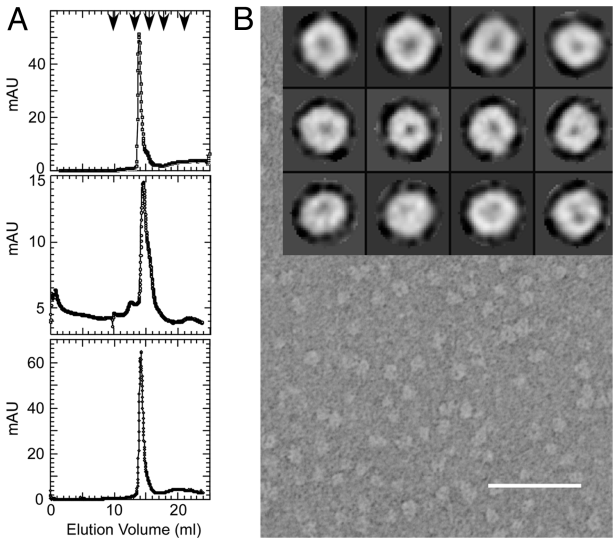

Fig. 2. In vitro characterization of his-tagged S^{21}68 and its derivatives. (*A*) Gel filtration of S^{21}68^{his} and derivatives. Purified protein was applied to a Superdex 200 column and analyzed as described in *Materials and Methods*. (*Top*) S^{21}68^{his}; (*Middle*) S^{21}68$_{\Delta TMD1}$^{his}; (*Bottom*) irsS^{21}68^{his}. Arrowheads indicate the protein standards, from left to right: 670, 158, 44, 17, and 1.35 kDa. (*B*) Electron micrograph of negatively stained S^{21}68^{his} purified in DDM. (Scale bar, 500 Å.) (*Inset*) Single particle averages for S^{21}68^{his} (top row), S^{21}68$_{\Delta TMD1}$^{his} (middle row), and irsS^{21}68^{his} (bottom row). Each single box is 148 × 148 Å.

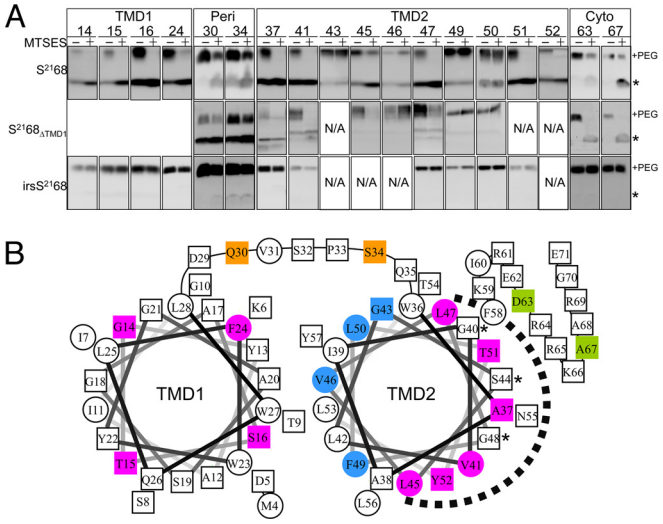

Fig. 3. MTSES protection analysis of S^{21}68. (*A*) Whole cells carrying plasmids encoding single-Cys substitutions of S^{21}68 or its derivatives were induced, treated with the nonpermeant thiol reagent MTSES, subjected to organic denaturation and delipidation, treated with PEG-maleimide, and analyzed by immunoblot, as described in *Materials and Methods*. The asterisk and "+PEG" indicate the position of the unmodified monomer and the PEGylated species, respectively. MTSES protection is indicated by an MTSES-dependent decrease in the PEGylated species and increase in the unmodified species. NA, not available; Peri, periplasmic loop; Cyto, cytoplasmic tail. (*B*) MTSES-protected positions in TMD2 map to its most hydrophilic face. Helical projections of TMD1 and TMD2 are shown, with hydrophobic residues as circles and hydroxylated, and hydrophilic residues, as well as Ala and Gly, as squares. Magenta and blue indicate transmembrane positions of S^{21}68 that do or do not show protection by MTSES. Also shown are the positions in the periplasmic loop (orange) and cytoplasmic tail (green) that show MTSES protection. The dashed arc indicates the deduced luminal face of TMD2. Asterisks, GxxxSxxxG motif in TMD2.

mutant allele with membrane-impermeant thiol reagent (2-sulfonatoethyl) methanethiosulfonate (MTSES). After quenching the reaction, cells are solubilized with SDS/urea, and the extent of MTSES modification is assessed by derivatizing the remaining free cysteines with a high molecular mass (5 kDa) derivative of methoxy-PEG maleimide. For the hole-forming *S^{21}* alleles, residues in both the periplasm and cytoplasm should be modified by MTSES, given a luminal diameter of at least the 6 Å needed for passage of the reagent through the bilayer (17). We first examined the accessibility of cysteines located in either the periplasmic loop or the cytoplasmic domain of S^{21}68. As can be seen in Fig. 3*A*, positions in the periplasmic loop of S^{21}68 (positions 30 and 34) show partial protection, as can be seen from comparing the unmodified species (asterisk) with or without MTSES, or by comparing the PEGylated species (+PEG), with or without MTSES. (The intensities of the unmodified and PEGylated forms cannot be directly compared with each other because of inherent differences in the efficiency of blot transfer and immunostaining.) For both irsS^{21}68 and S^{21}68$_{\Delta TMD1}$, the protection is much less efficient, possibly due to a difference in the membrane proximity of these residues in the different contexts. That is, in the WT protein, the periplasmic location of TMD1 may displace the loop residues from the bilayer. Importantly, the protection of the cytoplasmic C-terminal positions (63 and 67) is efficient for both the hole-forming alleles, S^{21}68 and S^{21}68$_{\Delta TMD1}$, but undetectable for the lysis-defective irsS^{21}68. Also, membrane depolarization by 2,4-dinitrophenol (DNP) has no effect on the irsS^{21}68 C-terminal inaccessibility to MTSES (Fig. S2). Together with previous findings, we conclude that (*i*) the cytoplasmic membrane of cells expressing *irsS^{21}68* retains its

impermeability to MTSES, and (*ii*) the lumen of pinholes formed by both $S^{21}68$ and $S^{21}68_{\Delta TMD1}$ is large enough to permit the diffusion of MTSES into the cytoplasm.

Identification of the TMD2 Residues Lining the $S^{21}68$ Channel. Because MTSES penetrates the lesion formed by $S^{21}68$, it was feasible to use the cysteine-scanning-accessibility method outlined above to determine which face of the TMD2 helix faces the lumen of the pinhole. Single cysteines were engineered along the length of TMD2 helices encoded by *$S^{21}68$*, *$irsS^{21}68$*, and *$S^{21}68_{\Delta TMD1}$* (Fig. 1*A*). With one exception, $S^{21}68_{S44C}$, none of the mutants changed function. MTSES did not react with any of irsS^{21}68 proteins carrying cysteine substitutions in TMD2, which is consistent with its inability to form holes in the cytoplasmic membrane (Fig. 3*A*; Fig. S2). By contrast, in both $S^{21}68$ and $S^{21}68_{\Delta TMD1}$, the same positions lining the hydrophilic face of TMD2 were found to be accessible to MTSES (Fig. 3 *A* and *B*), suggesting that these residues face the lumen of the pinhole. The behavior of the lysis-defective mutant $S^{21}68_{S44C}$ confirms the linkage between MTSES-sensitivity and lethal pinhole formation. Although located in the hydrophilic face, $S^{21}68_{S44C}$ lost MTSES-accessibility, even when the membrane was depolarized (Figs. S2 and S3). However, when coexpressed with $S^{21}68$, triggering occurred very early and it became MTSES-accessible (Fig. S3).

SAR Domain of $S^{21}68$ Is in the Periplasm. Next, cysteine was substituted for four residues which would occupy the different helical faces of TMD1. In the $S^{21}68$ context, all four positions were found to be accessible to MTSES (Fig. 3*A*). These results extend our previous results that, during the pathway to pinhole-formation, TMD1 becomes protease-sensitive in spheroplasts (7), and indicate that it becomes completely relocated to the aqueous milieu of the periplasm, rather than just to the external face of the cytoplasmic membrane. In contrast, the same positions in the nonlethal *irs*-tagged derivative were completely insensitive to MTSES, consistent with its retention in the membrane.

Cross-Linking of the Pinholin in the Membrane and in Detergent. To identify the oligomeric states of $S^{21}68$ and its derivatives, whole cells expressing *$S^{21}68$* or *$irsS^{21}68$* were treated with the membrane-permeable amine-specific cross-linker, dithiobis[succinimidyl propionate] (DSP) and analyzed by immunoblot using anti-S^{21} antibodies. For $S^{21}68$, a cross-linked ladder up to at least hexameric order was obtained (Fig. 4, lane 2). In contrast, oligomerization appeared to be blocked at the dimer stage in cells expressing the nonlethal *$irsS^{21}68$* (lane 3). Also, we have previously shown that the presence of the *irs* epitope on $S^{21}68$ not only renders the protein nonfunctional, but also converts it to an antiholin, which blocks the hole-forming activity of $S^{21}68$ (7). Accordingly, when *$S^{21}68$* and *$irsS^{21}68$* were coexpressed, the formation of cross-linked oligomers of $S^{21}68$ above the dimeric species was inhibited (lane 4). These data demonstrate that the cross-linking ladder generated from treating whole cells can be correlated with the lytic function of the pinholins present. The DSP cross-linking pattern for purified $S^{21}68$ in detergent was similar to that obtained from the membrane-embedded protein, except that, including the monomer, seven species were clearly identifiable (Fig. 4, lane 5), each with an Mr corresponding to an integral multiple of the Mr of the monomer (Fig. S4). The same multimer ladder, shifted for the reduced molecular mass of the monomer, was seen for the other lytic allele, $S^{21}68_{\Delta TMD1}$, as well as for the nonlytic irsS^{21}68, which, in the absence of the membrane, has no barrier to pinhole formation (Fig. 4, lanes 6 and 7).

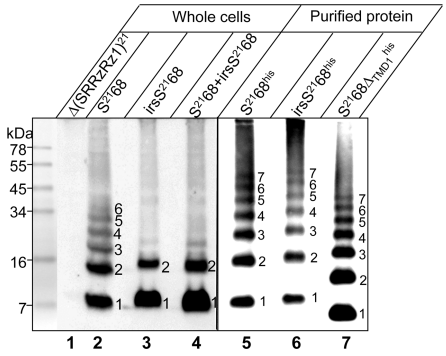

Fig. 4. DSP cross-linking reveals pinholin oligomerization in vivo and in vitro. (*Left*) Whole cells carrying prophage $\lambda Q^{21}\Delta(SRRzRz1)^{21}$ only (lane 1), or prophage $\lambda Q^{21}\Delta(SRRzRz1)^{21}$ with either plasmid pS^{21}68 (lane 2), pirsS^{21}68* (lane 3), or prophage $\lambda S^{21}68$ with the plasmid pirsS^{21}68* (lane 4), as indicated, were induced, treated with the cross-linker DSP, and analyzed by SDS/PAGE and immunoblot, as described in *Materials and Methods*. (*Right*) Protein purified from expression of alleles encoding his-tagged S^{21}68 or its derivatives, as indicated, was treated with DSP and analyzed by immunoblot. Oligomeric state indicated for each cross-linked species.

Pinhole Arrangement Is Suggested by Computational Modeling. Because its lethality drastically limits the level of protein expression, the pinhole is currently not amenable to high-resolution structural analysis by crystallography or NMR. However, the simplicity of $S^{21}68_{\Delta TMD1}$, comprising little more than a single transmembrane helix, and the fact that it forms holes with the same lumen-facing residues as the full-length holin, suggested a computational approach could be used to complement the biochemical and ultrastructural investigations. Therefore, a sequence corresponding to residues 36–58 of TMD2 was used in a simulated annealing search for closed N-mers, varying N from 5 to 7, and the resulting structures evaluated according to two general criteria. First, the distribution of MTSES-insensitive residues (43, 46, 49, and 50), which should be facing the lipid, and MTSES-sensitive residues (37, 41, 45, 47, 51, and 52), which should be facing the lumen. Second, the size of the predicted transmembrane pore, which must be large enough to allow both passage of MTSES through the membrane and allow the chemistry of MTSES labeling without steric clash. The structures obtained for $n = 5$–7 all gave lipid-lumen distributions that were compatible with the experimental results, with the exception of Leu47, which, although MTSES-sensitive, was always lipid-exposed, not lumen-facing. However, Leu47 lipid exposure was somewhat attenuated in the heptameric structure (Fig. 5), in that only the delta carbons were lipid-exposed in this bundle, and the remaining atoms of the side chain (e.g., C_β and C_γ) were involved in helix–helix interactions that are juxtapositioned to the lumen surface of the pinhole. The pore-size criterion significantly favored the heptamer model, where the diameter of the luminal cavity is ≈15.3 Å at Val41, constricting to 13.3 Å at Leu45 in the center, and opening up to 16.0 Å at Thr51 (Fig. 5). These dimensions are significantly larger than in the hexamer (7–13 Å) and pentamer (≈6 Å) (Fig. S5). Because MTSES occupies an ≈12 × 6 Å cylindrical space (18), only the hexamer and heptamer structures are compatible with MTSES permeation, and the hexameric lumen would likely put unacceptable steric constraints on MTSES reactivity toward luminal thiols. Together, the simulated annealing computations favor a model for the functional pinhole based on a heptameric bundle of TMD2 helices, consistent with the results obtained with treating the purified pinholes with the cross-linker DSP (Fig. 4).

Using the energy function in the CHI software suite (see *Materials and Methods* for details), we identified 20 residues involved in helix–helix interactions in the heptamer, which, by

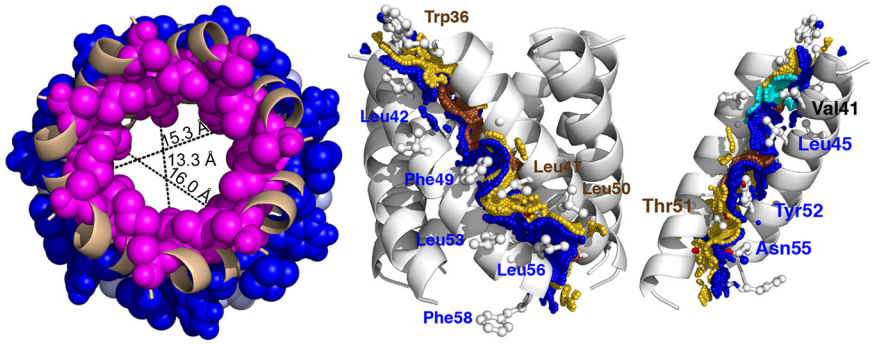

Fig. 5. Computational model for the heptameric pinhole. (*Left*) Top down view of $n = 7$ pinhole model with pore distances shown at various depths. MTSES-sensitive and insensitive positions are shown in magenta and blue, respectively. (*Center*) Side view of $n = 7$ pinhole model showing the helix–helix interaction contact surface. Contact surface A containing the glycine zipper is shown in gold and labeled in brown; the Gly40, Ser44, and Gly48 contact surface is colored brown. Contact surface B is shown and labeled in blue. (*Right*) A luminal view of the contact surface, with five helices removed for clarity. Contact surfaces are colored as in *Center*, except that Val41 is shown in cyan.

occluded surface analysis (19, 20), led to the assignment of two interaction surfaces could for each helix: surface A, comprising residues $W_{36}A_{37}xxG_{40}V_{41}xG_{43}S_{44}xxL_{47}G_{48}xL_{50}T_{51}xxT_{54}$; and surface B, comprising residues $A_{38}xxV_{41}L_{42}xxL_{45}xxxF_{49}xxY_{52}L_{53}xN_{55}L_{56}xF_{58}$ (Fig. 5). Val41 has a unique role in the pinholin, because it has significant interactions on the inner surface of the pore in both the A and B faces. Interestingly, the core of surface A is formed by a triplet of small residues, $G_{40}xxxS_{44}xxxG_{48}$, which makes a sterically unhindered pocket accommodating the side chains of the bulky residues L45, F49, and Y52. The heptamer structure also displays three interhelical hydrogen bonds between Ser or Thr side chains and backbone carbonyls on different helices: (*i*) Ser44/Leu45; (*ii*) Thr51/Tyr52; and (*iii*) Thr54/Leu56.

Discussion

The pinholins are a new class of holins that forms small holes using only a single TMD (7). Interest in the prototype pinholin, $S^{21}68$, was piqued by the simplicity of its primary structure, by evidence indicating that its N-terminal TMD was required to exit the bilayer for triggering to occur, and by its near identity with the holin of the prophage 933w, which controls release of Stx toxin during *E. coli* O157:H7 infections (Fig. S6) (10, 11). Here, we have used structural, biochemical, and computational studies to interrogate the structure of the lethal pinholin lesion, both in the membrane and purified in detergent.

Topological Dynamics and Pinhole Formation in the Membrane. The picture that TMD1 exits the membrane during the hole-formation pathway has been strongly reinforced here, with the finding that in $S^{21}68$, which triggers, but not in $irsS^{21}68$, which does not, residues all around the TMD1 helix become sensitive to MTSES attack in whole cells (Fig. 3*A*). Also, it was shown that coupled to this topological change in TMD1, positions along one surface of TMD2 and in the C-terminal cytoplasmic tail become accessible to MTSES (Fig. 3*A*). Not unexpectedly, the surface of $S^{21}68$ that becomes solvent-exposed is its most hydrophilic surface (Fig. 3*B*). Although the arc of accessibility begins and ends with Leu residues (L45, L47), all but one (V41) of the other residues on that face are either polar (N55), hydroxylated (S44, T51, and Y52), or of neutral hydrophobicity (A37, G40, and G48). Importantly, protection for most of the lumen-facing residues approaches completion (Fig. 3*A*), indicating that essentially all of the $S^{21}68$ protein, which is present in ≈6,400 copies per cell at the time of triggering, based on quantitative immunoblotting with purified $S^{21}68$ as a standard (Fig. S7), is involved in pinholes. Also, the DSP-cross-linking data clearly indicate that oligomeric complexes of $S^{21}68$ up to at least hexamer order are present in the membrane after triggering (Fig. 4). In contrast, if TMD1 is prevented from exiting the membrane by the *irs* tag, thus, blocking pinhole formation, DSP-cross-linking indicates that the protein cannot oligomerize beyond a dimer. Thus, the pinhole formation system seems to be set up for an all-or-nothing response that suddenly forms ≈900 pinholes. Although we do not know the ion flux the pinholes would support, they must be sufficiently large to permit efficient MTSES reaction with luminal thiols, which would certainly require at least 1-nm diameter (18). Because single colicin channels of ≈0.8-nm diameter can depolarize an *E. coli* cell in a few minutes (21, 22), it seems likely that >900 heptameric pinholes is greatly in excess of what is needed for depolarization within seconds. We suggest that this result reflects the biological mandate for a pinholin to effect instantaneous and complete deenergization of the membrane at the programmed time; thus, causing quantitative activation of the prelocalized SAR endolysins and rapid lysis. It would be counterproductive to form pinholes gradually, which would presumably reduce ATP-generation and the biosynthetic capacity of the infected cell in parallel.

Structure of the Pinhole. The pinholes are too small to visualize in membranes where triggering has occurred, so our only direct structural information in the biological context comes from the thiol accessibility and cross-linking data described above. However, the pinhole can be purified in DDM as a holo-heptameric complex (Figs. 2 and 4). Also, searches using simulated annealing of TMD2 generated a heptameric model for the pinhole that is consistent with all of these results. Importantly, one of the two heterotypic interaction surfaces in the heptameric model contains the sequence $G_{40}xxxS_{44}xxxG_{48}$. The motif appears to be critical for pinhole formation, because one of the single Cys substitutions used in this study, S44C, does not trigger. Also, similar motifs are conserved in TMD2 in other holins likely to be pinholins, some not detectably related to $S^{21}68$ (Fig. S6). Such "glycine-zipper" motifs featuring Gly and other residues with small side chains at intervals of 3 amino acids underlie the heterotypic interactions between TMDs in the other well-studied homo-oligomeric channel proteins: KcsA (tetramer), MscL (pentamer), VacA (hexamer), and MscS (heptamer) (23). In each of these cases, the homo-oligomerizing helix using this motif is the sole TMD that lines the pore, and, as in our model for the heptameric pinhole, the interaction is heterotypic, with the motif embedded in one face that interacts with a different face of the next helix. Last, it must be noted that the GxxxGxxxG motif was first identified in the homotypic dimer interaction surface between the TMDs of glycophorin (24), and has recently been shown to mediate homotypic dimerization of the TMD of myelin protein zero (MPZ), both in membranes and in detergent (25).

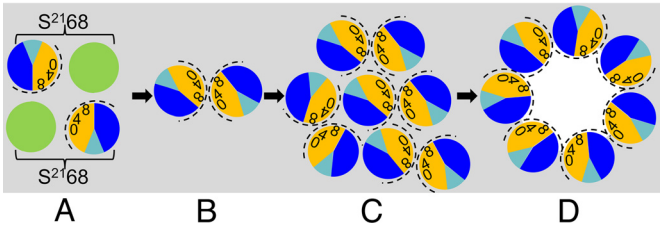

Fig. 6. Model for the pinhole formation pathway. View is top-down from periplasm; gray, lipid. TMD1 and TMD2 are shown as green and sectored circles, respectively. In TMD2, orange and dark blue represent A and B interaction faces (Fig. 5), with 0, 4, and 8 indicating the helical positions of the G_{40}, S_{44}, and G_{48} residues, respectively. The face accessible to MTSES in the pinhole is indicated by the dashed arc. (*A*) Inactive dimers, with bracket linking cognate TMD1 and TMD2; one possible orientation is shown. (*B*) Active dimers, after escape of TMD1 from membrane; homotypic interface. (*C*) Aggregate of active dimers; actual number of dimers is likely to be much larger. (*D*) Heptameric pinholes after triggering; heterotypic interface.

Implications for the Prehole State and Holin Triggering. Together, the MTSES-protection patterns, chemical cross-linking data, and computational results suggest a general model for the hole-formation pathway. In this perspective, the pinholins accumulate as dimers, randomly dispersed in the membrane; these dimers are inactive because TMD1 is still in the bilayer (Figs. 1*B* and 6). We have shown that, in a population of pinholins, TMD1 gradually exits the membrane, with the proportion increasing as the triggering time approaches (7). The release of TMD1 leads to formation of the active dimers (Figs. 1*B* and 6), with only TMD2 in the bilayer; obviously, the ΔTMD1 protein would accumulate directly in this conformation. In the active dimer, we suppose that the hydrophilic face of TMD2 is sequestered against itself with the $G_{40}xxxS_{44}xxxG_{48}$ motif supporting a homotypic interface. When a critical concentration of active dimers is reached, formation of 2D aggregates begins (Fig. 6). There is precedent for this model with bacteriorhodopsin (BR). BR accumulates as a monomer in the cytoplasmic membrane until a critical concentration (C_r) is reached, after which the free BR concentration remains constant and the hexagonally-packed BR lattice accumulates. In the pinholin aggregates, triggering would then result from a change in how TMD2 interacts with itself, shifting from the homotypic interaction defining the dimer to the heterotypic A:B interaction, also dependent on the zipper motif. The driving force for this conversion could be hydration of the luminal-side chains, which, in the heptameric model presented here, are mostly hydrophilic.

In this pathway, the prehole conformation is essential for pinhole formation, rather than just an inactive state. It should be noted that the S44C substitution is inactive in hole-formation, but can be recruited into pinholes by functional $S^{21}68$ (Fig. S3). We suggest that S44C disrupts the prehole active dimer by poisoning the homotypic interface, as it should in the central position of the GxxxSxxxG motif, but can be accommodated in the heterotypic interface. Thus, the mutant protein would be incorporated into holes by being a proximal monomeric bystander when the concerted triggering event occurs.

This model does not directly address the sensitivity to the energized state of the membrane, which might oppose the hydration step, stabilize the GxxxSxxxG interaction, or destabilize the heterotypic interhelical interactions in the pinhole. In this regard, the helices of the modeled heptamer are aligned at an angle of 34° to the normal, a geometry that might be strongly affected by the presence of the membrane potential (Fig. 5). The sensitivity to the proton motive force (pmf) is a key component of the biological function of the pinholin, and indeed all holins, because it confers "all or nothing" character. In our rationale, the spontaneous conversion of a single aggregate of pinholin dimers to a pinhole leads immediately to pmf collapse, assuring coordinated holin triggering throughout the whole cell. In any case, the structural and biological model presented here provides a framework for future experiments to examine the working parts of this simple, universal, and ancient biological timing system.

Materials and Methods

General Methods. Bacterial culture growth, plasmids and prophage construction, and general DNA manipulations are described in *SI Materials and Methods*. In general, *$S^{21}68$* was expressed from plasmid $pS^{21}68$, which carries the modified phage 21 lysis gene cassette, genes (*SRRzRz1*)^{21} (26) under its native promoter pR'^{21}. The other lysis genes were inactivated by nonsense mutations, so that only *$S^{21}68$* is expressed. Similarly, the *$irsS^{21}68$* and *$S^{21}68_{\Delta TMD1}$* alleles are expressed from plasmids $pirsS^{21}68$ and $pS^{21}68_{\Delta TMD1}$, respectively, which are of the same construction as $pS^{21}68$, except that the promoter is pR′ from phage lambda. The $pS^{21}68$ is transactivated by the phage 21 late gene activator, Q^{21}, provided by the thermal-inducible prophage $\lambda Q^{21}\Delta$(*SRRzRz1*)^{21}. Both $pirsS^{21}68$ and $pS^{21}68_{\Delta TMD1}$ are transactivated by lambda Q, provided by the plasmid pQ, a low-copy plasmid in which *Q* is under the control of an IPTG-arabinose inducible promoter (27). For experiments requiring coexpression of the WT *$S^{21}68$* with certain derivative alleles, prophage *$\lambda S^{21}68$* was used to provide one *$S^{21}68$* allele and Q^{21}, which transactivates plasmids $pS^{21}68_a$ or plasmid $pirsS^{21}68$*. Single-cysteine substitutions were inserted in corresponding plasmids by site-directed mutagenesis. Bacterial strains, prophages and plasmids are listed in Table S1. Structures of key plasmids and phages are in Fig. S8.

Purification and Gel Filtration Chromatography of $S^{21}68^{his}$ and Its Variants. For all experiments involving purified protein, alleles encoding his-tagged *S^{21}* gene products were used, with the sequence GGH_6GG inserted between residues 66 and 67 (7). The presence of the oligohistidine tag had no effect on function or oligomerization (Fig. S9). $S^{21}68^{his}$, $S^{21}68_{\Delta TMD1}{}^{his}$, and $irsS^{21}68^{his}$ were purified from an induced culture of *E. coli* C43(DE3) (28), carrying the plasmid $pETS^{21}68^{his}$, $pETS^{21}68_{\Delta TMD1}{}^{his}$, and $pETirsS^{21}68^{his}$, respectively. Induction, detergent extraction, and purification of the his-tagged proteins by immobilized metal affinity chromatography have been described (29) and can be found in *SI Materials and Methods*. $S^{21}68^{his}$ and its variants were eluted in buffer containing 20 mM Tris, pH 7.9/150 mM NaCl/500 mM imidazole/0.1% (wt/vol) DDM. Purified protein samples were analyzed by gel filtration using a Superdex 200 10/300 GL column (Amersham Pharmacia) on an AKTA FPLC workstation (Amersham Pharmacia) (*SI Materials and Methods*). Protein standards were purchased from Bio-Rad and used according to the manufacturer's instructions.

Electron Microscopy. Purified protein at 0.5 μM was applied to freshly glow-discharged formvar-carbon coated grids and stained with 2% (wt/vol) aqueous uranyl acetate according to the method of Valentine et al. (30). Micrographs were recorded on a JEOL 1200EX TEM operating at 100 KV, with a calibrated magnification of 48,600×, and scanned on a Leafscan 45 microdensitometer to a final sampling size of 4.12 Å per pixel at the specimen level. ≈900 particles for $S^{21}68^{his}$, 1,100 particles for $S^{21}68_{\Delta TMD1}{}^{his}$, and 710 particles for $irsS^{21}68^{his}$ were selected manually, low-pass filtered to remove high-frequencies beyond 10 Å, and subjected to iterative, reference-free classification using the refine2d.py command in the EMAN (31) software package.

Cysteine Modification. Cultures were grown to A_{550} = 0.4, induced with IPTG/arabinose or by a thermal shift, as appropriate, and aerated past the time of holin triggering or, in the case of nonlethal *$S^{21}68$* alleles, for 50 min. Cells corresponding to 0.25 A_{550} units were collected by centrifugation, washed twice with 1 mL PB (50 mM phosphate buffer, pH 7), and then resuspended in 0.25 mL of PB. Each sample was divided into two 125 μL aliquots. To one, 10 mM MTSES (Anatrace) was added and to the other, an equivalent amount of water was added. After 30 min at room temperature, 50 mM L-cysteine was added to quench any unreacted MTSES. After 10 min, the cells were diluted by the addition of 0.75 mL PB, collected by centrifugation, washed twice with 1 mL PB, resuspended in 100 μL PB, and extracted with of 750 μL chloroform:methanol:water (1:4:1). After incubation on ice for 30 min, the denatured and delipidated proteins were collected by centrifugation at 13,000 × *g* for 5 min at 4 °C. The protein pellets were washed once with 400 μL 95% methanol and resuspended in 100 μL PEGylation buffer [10M urea/1% SDS/1 mM EDTA/0.6 M Tris, pH 7; adapted from Lu and Deutsch (32)]. Fifty μL of each sample was transferred to a clean tube and treated with 0.2 mM mPEG-maleimide (Creative Biochem) for 30 min at room temperature, and then precipitated with 1 mL cold ethanol. After overnight at −20 °C, proteins were

collected by centrifugation at 13,000 × *g* for 15 min at 4 °C. The pellets were air-dried and resuspended in sample loading buffer for analysis by SDS/PAGE (33). For experiments involving depolarization of the membrane, 1 mM DNP was added into the culture at the time of harvesting and used to supplement PB in each step until quenching with L-cysteine.

Chemical Cross-Linking. A culture volume corresponding to one A_{550} unit was harvested, washed and resuspended in 640 μL of PBS (PBS, containing 0.1 M sodium phosphate/0.15 M NaCl, pH 7.2), and treated with 2 mM DSP (Pierce) at room temperature for 30 min. The reaction was quenched by the addition of 20 mM Tris, pH 7.5, and the proteins were collected by precipitation with trichloroacetic acid for analysis by SDS/PAGE. For the DSP cross-linking of purified $S^{21}68^{his}$ or its variants, 1 pmol of each protein in 0.1% DDM was used. The reaction was mixed with 2× sample loading buffer directly after quenching, boiled for 5 min, and analyzed by SDS/PAGE.

SDS/PAGE and Western Blotting. SDS/PAGE and Western blotting was performed as described (7), and can be found in *SI Materials and Methods*; 10% Tris-Tricine gels were used to separate protein samples. An antibody raised in rabbit against the S^{21} C-terminal peptide KIREDRRKAARGE was used as primary antibody to detect S^{21} protein variants (12). Horseradish peroxidase-conjugated goat-anti-rabbit secondary antibody was from Pierce.

Computational Methods. A 24-residue sequence corresponding to residues 36–58 of the S^{21} TMD2 (WAAIGVLGSLVLGFLTYLTNLYF; Fig. 1*A*) was used to compute oligomeric pinholin structures using CHI. The simulated annealing search calculation protocols have previously been described in detail (34, 35), except that the CHI suite of scripts uses CNS to implement the molecular dynamics. The OPLS topology and parameter sets were used with all polar hydrogens included (36). CHI uses an implicit membrane solvent with a dielectric constant = 2.

Conformations of TMD2 oligomers ranging from $n = 4$–7 were independently generated in different computational searches. Each oligomeric state was symmetrically searched with a helix rotation angle, α, ranging from 0° to 360°, and a sampling step size of 5°, starting with both left- ($\Omega = 45°$) and right-handed crossing angles ($\Omega = -45°$). For each oligomer, four trials were carried out for each rotation and crossing angle conformation using simulated annealing of all atomic coordinates during which rotation- and crossing-angles were free to vary. The resulting 576 structures were analyzed to determine the final rotation and crossing angles. Clusters of low-energy structures were calculated by determining the frequency of structures appearing in a particular region of interaction space using a cutoff of 1.0-Å rmsd and a minimum requirement of 10 structures to define a cluster. An average structure for each cluster was calculated and evaluated for consistency with the experimental data on the MTSES sensitivity and pore size from permeability.

The A- and B- helix–helix interaction surfaces were identified for the experimentally compatible oligomeric structures by calculating the distribution of interchain interactions using the occluded surface algorithm (19, 20). The occluded surface can be thought of as the contacting molecular surface between two helices and is represented in Fig. 5 as a dot surface. Hydrogen bonding interactions were calculated using HBPLUS (37).

ACKNOWLEDGMENTS. This work was supported by the Public Health Service Grant GM27099 (to R.Y.), National Science Foundation Grant MCB0423807 (to K.G.F.), the Robert A. Welch Foundation, and the Program for Membrane Structure and Function at Texas A&M University.

1. Young R, Wang IN (2006) Phage Lysis. *The Bacteriophages*, ed Calendar R (Oxford Univ Press, Oxford), 2nd Ed, pp 104–126.
2. Berry J, Summer EJ, Struck DK, Young R (2008) The final step in the phage infection cycle: The Rz and Rz1 lysis proteins link the inner and outer membranes. *Mol Microbiol* 70:341–351.
3. Young R (2002) Bacteriophage holins: Deadly diversity. *J Mol Microbiol Biotechnol* 4:21–36.
4. Bläsi U, Young R (1996) Two beginnings for a single purpose: The dual-start holins in the regulation of phage lysis. *Mol Microbiol* 21:675–682.
5. Wang IN, Deaton J, Young R (2003) Sizing the holin lesion with an endolysin-beta-galactosidase fusion. *J Bacteriol* 185:779–787.
6. Xu M, Struck DK, Deaton J, Wang IN, Young R (2004) The signal arrest-release (SAR) sequence mediates export and control of the phage P1 endolysin. *Proc Natl Acad Sci USA* 101:6415–6420.
7. Park T, Struck DK, Deaton JF, Young R (2006) Topological dynamics of holins in programmed bacterial lysis. *Proc Natl Acad Sci USA* 103:19713–19718.
8. Park T, Struck DK, Dankenbring CA, Young R (2007) The pinholin of lambdoid phage 21: Control of lysis by membrane depolarization. *J Bacteriol* 189:9135–9139.
9. Xu M, et al. (2005) Disulfide isomerization after membrane release of its SAR domain activates P1 lysozyme. *Science* 307:113–117.
10. Wagner PL, et al. (2002) Bacteriophage control of Shiga toxin 1 production and release by *Escherichia coli*. *Mol Microbiol* 44:957–970.
11. Wagner PL, Waldor MK (2002) Bacteriophage control of bacterial virulence. *Infect Immun* 70:3985–3993.
12. Barenboim M, Chang CY, dib Hajj F, Young R (1999) Characterization of the dual start motif of a class II holin gene. *Mol Microbiol* 32:715–727.
13. Rosevear P, VanAken T, Baxter J, Ferguson-Miller S (1980) Alkyl glycoside detergents: A simpler synthesis and their effects on kinetic and physical properties of cytochrome c oxidase. *Biochemistry* 19:4108–4115.
14. VanAken T, Foxall-VanAken S, Castleman S, Ferguson-Miller S (1986) Alkyl glycoside detergents: Synthesis and applications to the study of membrane proteins. *Methods Enzymol* 125:27–35.
15. Aoudia M, Zana R (1998) Aggregation behavior of sugar surfactants in aqueous solutions: Effects of temperature and the addition of nonionic polymers. *J Colloid Interface Sci* 206:158–167.
16. Strop P, Brunger AT (2005) Refractive index-based determination of detergent concentration and its application to the study of membrane proteins. *Protein Sci* 14:2207–2211.
17. Akabas MH, Stauffer DA, Xu M, Karlin A (1992) Acetylcholine receptor channel structure probed in cysteine-substitution mutants. *Science* 258:307–310.
18. Kaplan RS, et al. (2000) The yeast mitochondrial citrate transport protein. Probing the secondary structure of transmembrane domain iv and identification of residues that likely comprise a portion of the citrate translocation pathway. *J Biol Chem* 275:12009–12016.
19. Pattabiraman N, Ward KB, Fleming PJ (1995) Occluded molecular surface: Analysis of protein packing. *J Mol Recognit* 8:334–344.
20. Fleming KG, Engelman DM (2001) Computation and mutagenesis suggest a structure for the synaptobrevin transmembrane dimer. *Proteins* 45:313–317.
21. Schein SJ, Kagan BL, Finkelstein A (1978) Colicin K acts by forming voltage-dependent channels in phospholipid bilayer membranes. *Nature* 276:159–163.
22. Davidson VL, Brunden KR, Cramer WA, Cohen FS (1984) Studies on the mechanism of action of channel-forming colicins using artificial membranes. *J Membrane Biol* 79:105–118.
23. Kim S, et al. (2005) Transmembrane glycine zippers: Physiological and pathological roles in membrane proteins. *Proc Natl Acad Sci USA* 102:14278–14283.
24. Russ WP, Engelman DM (2000) The GxxxG motif: A framework for transmembrane helix-helix association. *J Mol Biol* 296:911–919.
25. Plotkowski ML, et al. (2007) Transmembrane domain of myelin protein zero can form dimers: Possible implications for myelin construction. *Biochemistry* 46:12164–12173.
26. Bonovich MT, Young R (1991) Dual start motif in two lambdoid *S* genes unrelated to lambda *S*. *J Bacteriol* 173:2897–2905.
27. Gründling A, Manson MD, Young R (2001) Holins kill without warning. *Proc Natl Acad Sci USA* 98:9348–9352.
28. Miroux B, Walker JE (1996) Over-production of proteins in *Escherichia coli*: Mutant hosts that allow synthesis of some membrane proteins and globular proteins at high levels. *J Mol Biol* 260:289–298.
29. Savva CG, et al. (2008) The holin of bacteriophage lambda forms rings with large diameter. *Mol Microbiol* 69:784–793.
30. Valentine RC, Shapiro BM, Stadtman ER (1968) Regulation of glutamine synthetase. XII. Electron microscopy of the enzyme from *Escherichia coli*. *Biochemistry* 7:2143–2152.
31. Ludtke SJ, Baldwin PR, Chiu W (1999) EMAN: Semiautomated software for high-resolution single-particle reconstructions. *J Struct Biol* 128:82–97.
32. Lu J, Deutsch C (2001) Pegylation: A method for assessing topological accessibilities in Kv1.3. *Biochemistry* 40:13288–13301.
33. Tran TA, Struck DK, Young R (2007) The T4 RI antiholin has an N-terminal signal anchor release domain that targets it for degradation by DegP. *J Bacteriol* 189:7618–7625.
34. Adams PD, Arkin IT, Engelman DM, Brunger AT (1995) Computational searching and mutagenesis suggest a structure for the pentameric transmembrane domain of phospholamban. *Nat Struct Biol* 2:154–162.
35. Adams PD, Engelman DM, Brunger AT (1996) Improved prediction for the structure of the dimeric transmembrane domain of glycophorin A obtained through global searching. *Proteins* 26:257–261.
36. Jorgensen WL, Tirado-Rives J (1988) The OPLS [optimized potentials for liquid simulations] potential functions for proteins, energy minimizations for crystals of cyclic peptides and crambin. *J Am Chem Soc* 110:1657–1666.
37. McDonald IK, Thornton JM (1994) Satisfying hydrogen bonding potential in proteins. *J Mol Biol* 238:777–793.